| | | |
|---|---|---|
| ESRF | **Experiment title:**<br>**Exploring the structural phase diagram of $Eu_{1-x}Ca_xTiO_3$ thermoelectric materials at different length scales using High resolution XRPD and Pair Distribution Function analysis** | **Experiment number**:<br>**CH-5342** |
| **Beamlines**:<br>ID22<br>ID15A | **Date of experiment**:<br>from: 18/04/2018 to: 23/04/2018<br>from: 21/04/2018 to: 24/04/2018 | **Date of report**:<br>31.08.2020 |
| **Shifts:**<br>18 | **Local contact(s)**:<br>CODURI Mauro (ID22); VAUGHAN Gavin (ID15) | *Received at ESRF:* |


**Names and affiliations of applicants** (* indicates experimentalists):

**Marco Scavini*, Carlo Castellano*, Stefano Checchia***
Università degli Studi di Milano, Dip. di Chimica, Milano, Italy;

**Marc Widenmeyer*[1], Songhak Yoon[2], Anke Weidenkaff[1,2], Xingxing Xiao[1]**
University of Stuttgart, Institute for Materials Science, Heisenbergstr. 3, 70569 Stuttgart, Germany;
Present Addresses:
[1] Technical University of Darmstadt, Department of Materials and Earth Sciences, Alarich-Weiss-Str. 2, 64287 Darmstadt, Germany
[2] Fraunhofer Research Institution for Materials Recycling and Resource Strategies IWKS, Aschaffenburger Str. 121, 63457 Hanau, Germany


## Report

### 1. Introduction

$Eu_{1-x}Ca_xTiO_{3-\delta}$ solid solutions are novel and promising thermoelectric (TE) materials produced in pure form by the proponent group. Partial substitution of $Ca^{2+}$ for $Eu^{2+}$ results in interesting physical properties, because the lattice thermal conductivity $\kappa_L$ decreases dramatically, while the electrical conductivity $\sigma$ is significantly enhanced at RT leading together to an increased figure of merit $ZT$.**[Xiao18]** The latter effect is linked to additional point defects formation that increases the charge carrier concentration.**[Xiao18]** Possible explanations for the huge reduction of $\kappa_L$ are, *e.g.*, the "rattling" of $Ca^{2+}$ in the $AO_{12}$ cuboctahedron due to the much smaller ionic radius of $Ca^{2+}$ leading to underbonded $Ca^{2+}$ cations or local symmetry breaks in respect to the average structure. Both structural modifications should deeply affect the phonon scattering rate.

In order to understand the physical properties of $Eu_{1-x}Ca_xTiO_{3-\delta}$ solid solutions, an accurate determination of their crystal structure at different length scales is vital to any further investigation on this novel and promising TE materials to reveal the $T$-$x$ stability ranges of different structures and the mechanism of phonon scattering. Despite this, no crystallographic study on this solid solution as a function of $T$ and $x$ (the structural phase diagram) is present in the literature.

The aim of this experiment was to establish the previously unstudied structural phase diagram of $Eu_{1-x}Ca_xTiO_{3-\delta}$ as well as the local deviations from the average structure, in order to relate the TE properties to their structure.

Data collected during experiment CH-5342 have been partially published by the proponent group in Refs.**[Xiao18, Widenmeyer20]**

## 2. Samples

$Eu_{1-x}Ca_xTiO_{3-\delta}$ solid solutions (where $x$ = 0.1, 0.2, 0.3, 0.4, 0.5, 0.6, 0.7, 0.8, 0.9) were synthesized using a modified Pechini method followed by annealing the samples at 1273 K and sintering at 1623 K-1673 K for 10 h under reducing conditions (10% vol. $H_2$ in $N_2$) as described in Ref.**[Xiao18]** and references therein.

## 3. Data collection strategy

High resolution Powder X-Ray Diffraction (PXRD) data were collected at the ID22 beamline of the ESRF on powdered samples of $Eu_{1-x}Ca_xTiO_{3-\delta}$ ($x$ = 0.1, 0.2, 0.3, 0.4, 0.5, 0.6, 0.7, 0.8, 0.9) using an X-ray wavelength $\lambda$ = 0.35439(1) Å and a 9-element detector array. A cryostream and a blower were used to collect patterns in low (100 K – 423 K) and high (373 K – 1268 K) temperature ranges, respectively. Data were collected in a wide $Q$ range (up to 12.5 $Å^{-1}$) at fixed $T$ values (100 K, 200 K, 300 K, 373 K, 473 K, 573 K, 673 K, 873 K, 973 K, 1073 K, 1173 K, 1268 K) for Rietveld analysis. Fast patterns acquisition was applied in between couples of $T$ values while heating at 5 K/min to follow the unit cell parameter changes.

The same samples were also measured at the ID15@ESRF for PDF analysis. Powder samples were loaded into 0.7 mm diameter quartz glass capillaries and mounted on a goniometric head on top of a rotation stage of the ID15A beamline of ESRF at 320.7 mm distance from the detector, a Dectris Pilatus 2M CdTe. Wavelength was $\lambda$ = 0.123984 Å. Maximum value of momentum transfer used for PDF calculation was $Q_{max}$ = 25 – 26 $Å^{-1}$. Also PDF quality patterns were collected at fixed $T$ values (100 K, 300 K, and 973 K) and also while heating at 5 K/min.

## 4. Brief description of the structural model of the $EuTiO_3$-$CaTiO_3$ system

The structure of the end members of the solid solution has been widely investigated. At room temperature, $EuTiO_3$ adopts the cubic undistorted perovskite structure (space group $Pm\bar{3}m$). In the cubic phase, the atomic sites are 1*a* Ti (0, 0, 0); 1*b* Eu/Ca (½, ½, ½); and 3*d* O (0, ½, 0). $TiO_6$ octahedra share corners with six different $TiO_6$ units, while Eu ions fill the cuboctahedral sites forming $EuO_{12}$ units. Below ~ 235 K a cubic to tetragonal (space group $I4/mcm$) phase transition takes place **[Allieta12]** driven by the antiferrodistorsive tilting of $TiO_6$ octahedra along the $c$-axis ($a^0a^0c^-$ using the Glazer notation **[Glazer75]**). The tetragonal cell vectors $\boldsymbol{a}_o$, $\boldsymbol{b}_o$, and $\boldsymbol{c}_o$ are obtained starting from the perovskite ones $\boldsymbol{a}_p$ by the following axis transformations (1 1 0), (1 $\bar{1}$ 0), (0 0 2) and their moduli are $a_T = \sqrt{2}a_p$, $b_T = \sqrt{2}a_p$, and $c_T = 2a_p$. Each cell contains four $ABO_3$ formula units ($V_o = 4V_p$). $CaTiO_3$ takes the same undistorted perovskite structure only at very high $T$ values. Starting from the high temperature cubic phase, $CaTiO_3$ transforms into the tetragonal $I4/mcm$ space group around 1635 K and undergoes a further phase transition around 1512 K towards an orthorhombic space group $Pbnm$ ($a_o = \sqrt{2}a_p$, $b_o = \sqrt{2}a_p$, and $c_o = 2a_p$,) and is maintaining this last structure down to room temperature **[Ali05, Yashima09]**.

Using the setting of Ref.**[Baran96]**, in the orthorhombic phase the Ca ions are in 4*c* ($0+x_{Ca}$, $0+y_{Ca}$, ¼) site, the Ti ones are in 4*b* (0, 1/2, 0) site, while two different oxygen site exists: O(1) 4*c* ($0+ x_{O(1)}$, $½+y_{O(1)}$, ¼ ), O(2) 8*d* (¼ $+u$, ¼$+v$, $0+w$); this notation highlights the shifts of the atomic coordinates in respect to the same in the cubic phase. In $Pbnm$ the $TiO_6$ octahedra undergo an out-of-phase tilting with the same tilting amplitude $\phi_x$ (=

$\phi_y$) along *x*- and *y*-directions (which lie in the $\boldsymbol{a}_p$- $\boldsymbol{b}_p$-plane) and an in-phase-tilting along the *z*-direction $\phi_z$, along the $\boldsymbol{c}_p$-axis. This tilting architcture is defind as $a^-a^-c^+$, according to the Glazer tilt systems [Glazer75]. The tilting angles $\phi_x$ and $\phi_z$ are related to the *u*, *v*, *w* shifts of the equatorial O(2) atom by: $\phi_x = \tan^{-1} 4\sqrt{2}w$ and $\phi_z = \tan^{-1} 2(u + v)$.

## 5. Results:

In the following we will focus mainly on a subset of compositions (*x* = 0, 0.2, 0.4, 0.6, 0.8) and to the Rietveld refinements of high quality patterns collected at 100 K and 300 K. For the $EuTiO_3$ end member we refer to already published results **[Allieta12]**. Moreover, in case of $Eu_{0.8}Ca_2TiO_3$ we will describe in more details its unexpected structural modifications as a function of *T* that reveals the importance of studying the structural phase diagram at different length scales to gain a correct picture of this system.

Figure 1(a) reports a part of the XRD patterns collected at RT on all the selected samples about the cubic 220 reflection. The pattern of the *x* = 0.2 sample shows a single symmetric reflection in accordance to the cubic structure of this sample. On increasing the Ca concentration, the same reflection become asymmetric and splits indicating a phase transition to the orthorhombic structure. All the patterns have been fitted by means of Rietveld refinements to extract structural information (see e.g. Figs. 1(b) and 1(c)).

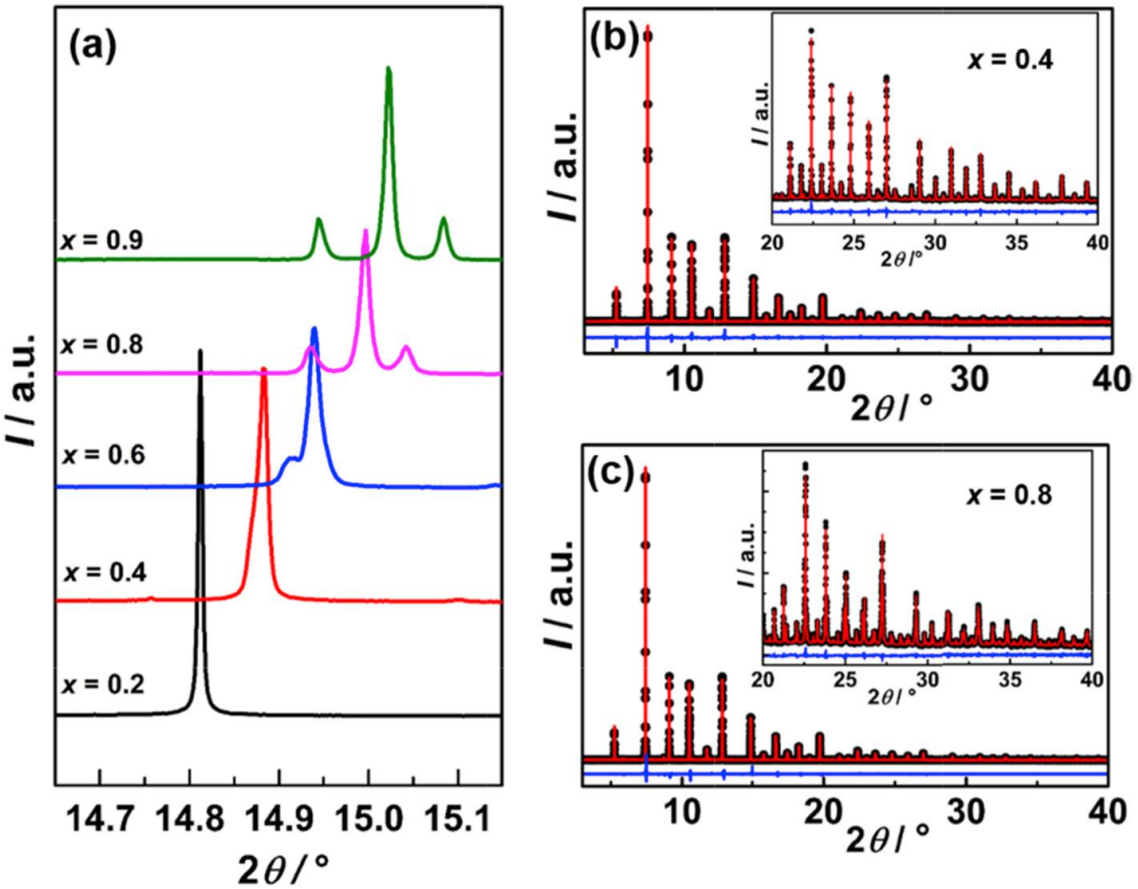


**Figure 1.** The powder X-ray diffraction patterns for $Eu_{1-x}Ca_xTiO_{3-\delta}$ samples, showing the progressive splitting of the cubic 220 reflection (a) and Rietveld refinements for the patterns of *x* = 0.4 (b) and *x* = 0.8 (c). See Ref.**[Xiao18]**

Figure 2 displays the fitted unit cell parameters (top panels), tilting angles as defined above (middle panels), and isotropic atomic means square displacement parameters: Atomic means square displacement parameters, Amsd (bottom panels).

Rietveld refinements reveal that the structure of the Ca-richest samples ($0.9 \geq x \geq 0.4$) is orthorhombic with space group *Pbnm* at both 100 K and 300 K. At both temperatures, on lowering Ca concentration the tilting angles decrease and eventually the system undergoes an orthorhombic to cubic phase transition: the $x = 0.2$ sample holds the undistorted perovskite structure. The structure of the $EuTiO_3$ end member is cubic at 300 K and tetragonal at 100 K **[Allieta12]**.

The analysis of the refined thermal parameters reveals that almost all Amsd values display smooth changes as a function of composition (see bottom panels of Figure 2). The only exception is exhibited by the oxygen Amsd parameter of the $x = 0.2$ sample, which is almost twice as large as the other values. This suggest that some structural disorder should exist at the local scale for this sample.

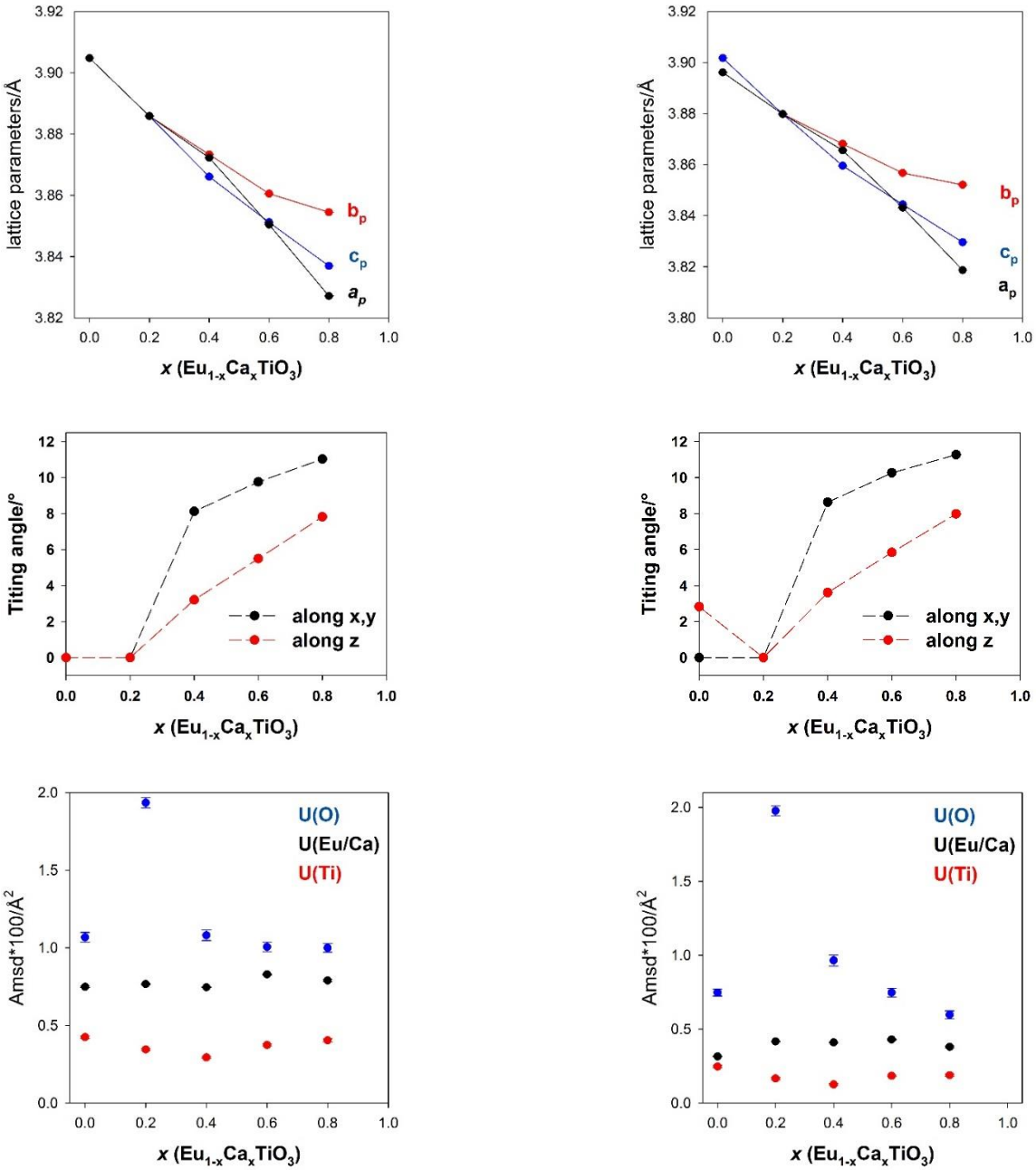


**Figure 2**. Selected results of the Rietveld refinements at RT (left panels) and 100 K (right panels) as a function of Ca concentration *x*. Top panels: unit cell parameters; for a better comparison between different phases, the pseudocubic parameters $a_p$, $b_p$, and $c_p$ are used; Middle panels: tilting angles, as defined in section 5. Bottom panels: Atomic means square displacement parameters (Amsd).

At 1268 K, *i.e*. at the highest *T* values reached during the experiment, only Eu-rich compositions ($x \leq 0.3$) have the cubic perovskite structure, while samples with $x \geq 0.4$ show either orthorhombic or tetragonal distortion, depending on composition.

$Eu_{0.8}Ca_{0.2}TiO_3$ shows a phase transition during heating from cubic (100 K < *T* < 592 K) to tetragonal on the long-range scale and back to cubic at *T* > 846 K. It should be stressed that the phase transition at *T* = 592 K is reversible.**[Widenmeyer20]** The PDF analysis of ID15 data allowed to relate this unexpected sequence of phase transitions to the local structure of $Eu_{0.8}Ca_{0.2}TiO_3$: at 100 K it is composed of a complex nanodomain arrangement of *Amm*2- and *Pbnm*-like local structures with different coherence lengths. The competition between ferroelectrically distorted octahedra (*Amm*2 as in $BaTiO_3$) and rigid, tilted octahedra (*Pbnm* as in $CaTiO_3$) results in a cubic long-range structure at low temperatures. The discrepancy between local and average scale leads to a peak in Amsd values for $Eu_{0.8}Ca_{0.2}TiO_3$ as shown in Fig.2. More detailed investigations are reported in ref. **[Widenmeyer20]**.

Some insight of the disorder at the local scale in the solid solutions $Eu_{1-x}Ca_xTiO_{3-\delta}$ come from the analysis of PDFs collected at ID15 beamline. Figure 3(a) reports the experimental *G*(*r*) function collected at RT on selected samples (light blue circles).The first and second *G*(*r*) peak at around 1.95 Å and 2.75 Å represent the nearest-neighbor Ti–O and *A*–O (*A* = Ca, Eu) distances, respectively; the third *G*(*r*) peak, around 3.3 Å, contains the *A*–Ti pairs. Local interatomic distances obtained by peak fits decrease more markly in respect to bond lengths obtained by Rietveld refinements passing from *x* = 0.2 to 0.9 (Fig. 3(b–d)). In particular, shorter and more broadly distributed *A*–Ti distances reflect the larger orthorhombic strain and the smaller unit cell volume obtained by introducing $Ca^{2+}$ into the solid solution. The contraction of Ti–O and *A*–O bond lengths at the local scale clearly exceeds the Vegard-like compositional dependence inferred from the long-range structures and is an indicator of the chemical pressure induced on both the *A*- and *B*-sites.

Applying different structural models to the *G*(*r*) curve in the compositional range of $0.2 \leq x \leq 0.9$ (red curves in Fig.3(a)) show that the extra contribution to locally stretched bond distances originates in the nature of the short-range distortions of Eu-rich samples. All *G*(*r*) curves are fitted up to *r* = 8 Å by a 2×2×2 supercell of the primitive cubic perovskite, in which atomic positions are refined within the symmetry constraints set by the *Pnma* space group, that is a differerent setting of *Pbnm* (both are n. 62), here chosen to get the *c*-axis unchanged while passing from the orthorhombic to the tetragonal structure.

The symmetry-decomposition of the refined *Pnma* phases into single-irrep distortion modes is shown in Fig. 3(e) and indicates which distortions contribute to the short-range structure at different compositions. The modes of Fig.3(e) are depicted schematically in Fig. 3(f). A detailed description of the modes analysis, is reported in ref.**[Xiao18]**.

The Ca-rich compositions ($x \geqslant 0.6$) are dominated by two octahedral tilt modes (belonging to irreps $R_4^+$ and $M_3^+$) by which rigid $TiO_6$ units rotate around one axis, accompanied by a scissor mode ($M_4^+$). The composition of these modes rationalizes the split, symmetric *A*–O peak observed in *x* = 0.8 and *x* = 0.9.

As *x* decreased, the octahedral tilt modes are replaced by a quadrupolar distortion ($M_1^+$) driven by *A*–site disorder and by an unconventional tilt ($X_5^+$), also accompanied by a scissor mode ($R_5^+$). Unlike rigid octahedral tilt modes, the $M_1^+$ quadrupolar distortion stretches all the out-of-plane *A*–O distances, forming the 4 + 8 distribution of distances observed in the *G*(*r*) for $x \leqslant 0.6$. Both $M_1^+$ and $X_5^+$ tend to form ordered short and long Ti–O distances, thus causing the Ti–O peak to be more smeared out at low-*x*. The longer Ti–O distances detected at the local scale (see Fig.3(b)) can be explained by considering that the distortion of the $TiO_6$ octahedra by the coupled $X_5^+$ and $R_5^+$ modes is needed to improve the *B*-site coordination sphere in absence of an octahedral tilt.

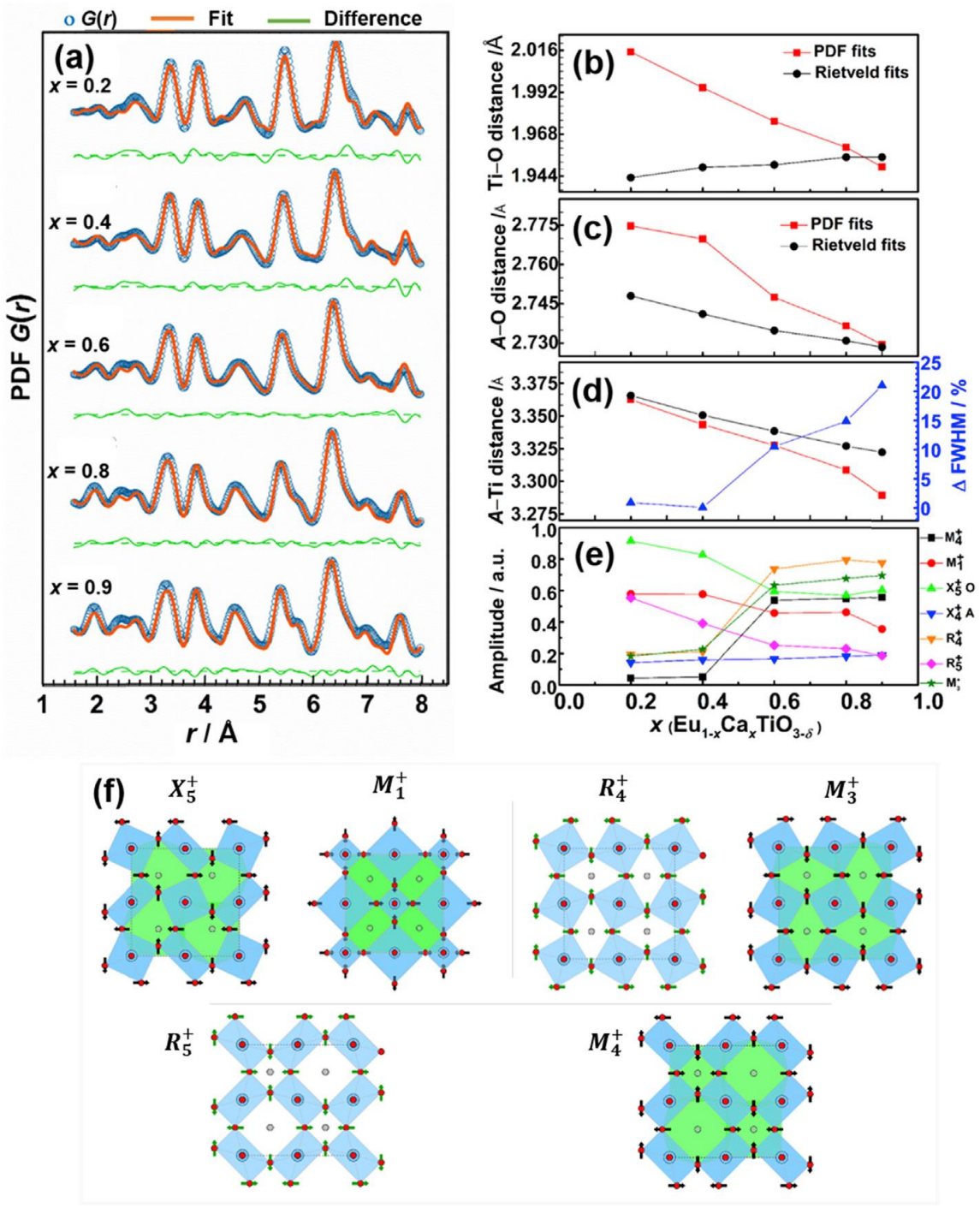


**Figure 3**. (a) Experimental PDF fitted by structural models with *Pnma* symmetry and fit residual curves with the respective mean values; (b,c) Ti-O, Ca/Eu-O, and Ca/Eu-Ti distances as inferred from the long-range models and from the respective PDF peaks; in (d), the change in full-width at half-maximum (FWHM) of the PDF peak with respect to the low-*x* minimum width is displayed; (e) normalized amplitudes of the mode intensities by comparing the undistorted perovskite structure with each refined structure obtained by PDF fits; (f) overview of the single distortions involving O atoms projected along the respective symmetry axes (red = O, blue = Ti, and grey = Ca/Eu = *A*); black arrows represent in-phase displacement along the symmetry axis; green arrows, out-of-phase along the symmetry axis; $TiO_6$ octahedra and $AO_{12}$ cuboctahedra are highlighted in light blue and green, respectively; the cuboctahedra not highlighted in green comprise both types of *A*-O patterns visible in a single plane. PDF, pair distribution function. From Ref.**[ Xiao18]**.

In summary, PDF analysis revealed the Ca-rich compositions ($x \geq 0.6$) are dominated by two local octahedral tilt modes observed also in the average structure; conversely, the pattern of an enhanced local distortion around *A*–cations appear in Eu-rich samples ($x \leq 0.4$), which stretches the Ti–O and *A*–O distances to a larger extent than observed by the reciprocal-space analysis.

**Outlook and future developments**

The high *Q*-resolution of the ID22 beamline coupled to the high energy and the fast data collection rate of ID15A beamline made it possible to study the mechanistic details of the crystal structural change of $EuTiO_3$-$CaTiO_3$ system at different length scales in a wide temperature range: 100 K ≤ *T* ≤ 1068 K, which is the *T* interval accessible using cryostream and blower as sample environments. Exploring this *T* range allowed to correlate the physical properties (in particular the thermoelectric ones) of $Eu_{1-x}Ca_xTiO_{3-\delta}$ compounds with their average and local structure. As an example, the observed coexistence of polar and tilted nanodomains in $Eu_{0.8}Ca_{0.2}TiO_3$ could be responsible for the obtained decrease of the lattice thermal conductivity $\kappa_L$ by giving the possibility for an enhanced phonon scattering rate. However, the latter requires further experimental verfification. As an outlook, it is anticipated to extend this investigation in order to complete the structural phase diagram of the $EuTiO_3$-$CaTiO_3$ system. On one hand, this would allow a complete analysis of all the phase transitions present in the system from the lowest *T* values, so saturating the order parameters of *Pbnm* distortion, up to the cubic perovskite structure. On the other hand, it would also reveal the origin of anomalies in the thermal conductivity of $Eu_{1-x}Ca_xTiO_{3-\delta}$ solid solutions recently detected at very low *T*.**[Xiao]**

**References**


**[Ali05]** R. Ali, M. Yashima, Space group and crystal structure of the perovskite $CaTiO_3$ from 296 to 1720 K, **Journal of Solid State Chemistry** 178 (2005) 2867–2872.

**[Allieta12]** M., M. Scavini, L. Spalek, V. Scagnoli, H. Walker, C. Panagopoulos, S. Saxena, T. Katsufuji, C. Mazzoli. Role of intrinsic disorder in the structural phase transition of magnetoelectric $EuTiO_3$, **Physical Review B85**, (2012) 184107.

**[Baran96]** A. Beran, E. Libowitzky, T. Armbruster, A single-crystal infrared spectroscopic and X-ray diffraction study of untwinned San Benito perovskite containing O H groups, **Canadian Mineralogist 34** (1996) 803.

**[Carpenter06]** M.A. Carpenter, C.J. Howards, K.S. Knight, Z. Zhang, Structural Relationships and a phase diagram for (Ca,Sr)$TiO_3$ perovskites, **J.Phys.: Condens. Matter 18** (2006) 10725-10749.

**[Glazer75]** A.M. Glazer, Simple ways of determining perovskite structures, **Acta crystallographica section A: crystal physics, diffraction, theoretical and general crystallography 31** (1975) 756–762.

**[Yashima09]** M. Yashima, R. Ali, Structural phase transition and octahedral tilting in the calcium titanate perovskite $CaTiO_3$, **Solid State Ionics 180** (2009) 120–126.

**[Widenmeyer20]** M. Widenmeyer , S. Checchia, X. Xiao, M. Scavini, A. Weidenkaff, Effects of Nanodomains on Local and Long-range Phase Transitions in Perovskite-type $Eu_{0.8}Ca_{0.2}TiO_{3-\delta}$, **Nanomaterials 10** (2020) 769

**[Xiao17]** X. Xiao, M. Widenmeyer, W. Xie, T. Zou, S. Yoon, M. Scavini, S. Checchia, Z. Zhong, P. Hansmann, S. Kilper, A. Kovalevsky, A. Weidenkaff, Tailoring the structure and thermoelectric properties of $BaTiO_3$ via $Eu^{2+}$ substitution, **Phys. Chem. Chem. Phys**. **19** (2017) 13469-13480.

**[Xiao]** X. Xiao, K. Philippi, M. Scavini, S. Checchia, M. Widenmeyer, W. Xie, Y. Liu, J. He, A. Weidenkaff, **paper in preparation**.

**[Xiao18]** X. Xiao, M. Widenmeyer, K. Mueller, M. Scavini, S. Checchia, C. Castellano, D. Ma, S. Yoon, W. Xie, U. Starke, K. Zakharchuk, A. Kovalevsky, A. Weidenkaff, A squeeze on the perovskite structure improves the thermoelectric performance of Europium Calcium Titanates, **Materials Today Physics 7** (2018) 96-105.